Structure and uncoating of immature adenovirus

Running title: Structure of immature adenovirus

Ana J. Pérez-Berná[1,†], Roberto Marabini[2,†], Sjors H. W. Scheres[1], Rosa Menéndez-Conejero[1], Igor P. Dmitriev[3], David T. Curiel[3], Walter F. Mangel[4], S. Jane Flint[5], and Carmen San Martín[1,*]

[1] Department of Macromolecular Structure, Centro Nacional de Biotecnología (CNB-CSIC), Darwin 3, 28049 Madrid, Spain

[2] Escuela Politécnica Superior, Universidad Autónoma de Madrid, Francisco Tomás y Valiente 11, 28049 Madrid, Spain

[3] The Gene Therapy Center, University of Alabama at Birmingham, Birmingham, AL 35294, USA.

[4] Biology Department, Brookhaven National Laboratory, Upton, New York 11973, USA

[5] Department of Molecular Biology, Princeton University, Princeton, NJ 08544, USA

† These authors contributed equally to this work

*Corresponding author:

Carmen San Martín.

Centro Nacional de Biotecnología (CNB-CSIC), Darwin 3, 28049 Madrid (Spain)

Ph: 34 91 585 5450, Fax 34 91 585 4506, e-mail: carmen@cnb.csic.es

Summary

Maturation via proteolytical processing is a common trait in the viral world, and is often accompanied by large conformational changes and rearrangements in the capsid. The adenovirus protease has been shown to play a dual role in the viral infectious cycle: (a) in maturation, as viral assembly starts with precursors to several of the structural proteins, but ends with proteolytically processed versions in the mature virion; and (b) in entry, because protease-impaired viruses have difficulties in endosome escape and uncoating. Indeed, viruses that have not undergone proteolytical processing are not infectious. We present the 3D structure of immature adenovirus particles, as represented by the thermosensitive mutant Ad2 *ts1* grown under non-permissive conditions, and compare it with the mature capsid. Our 3DEM maps at subnanometer resolution indicate that adenovirus maturation does not involve large scale conformational changes in the capsid. Difference maps reveal the location of unprocessed peptides pIIIa and pVI and help to define their role in capsid assembly and maturation. An intriguing difference appears in the core, indicating a more compact organization and increased stability of the immature cores. We have further investigated these properties by *in vitro* disassembly assays. Fluorescence and electron microscopy experiments reveal differences in the stability and uncoating of immature viruses, both at the capsid and core levels, as well as disassembly intermediates not previously imaged.

Keywords: Adenovirus, virus maturation, virus uncoating, virus structure, three-dimensional electron microscopy

Introduction

The icosahedral, non enveloped adenovirus capsid is composed of at least 11 different polypeptides plus the dsDNA genome. Crystal structures for only the major coat protein (hexon) and the vertex proteins (penton base and fiber) are available [1; 2; 3; 4]. The positions of minor capsid components IIIa, VI, VIII and IX in the virion have been defined by hybrid electron microscopy (EM) / X-ray crystallography studies [5; 6; 7; 8]. There is at present no detailed structural information about the disposition of DNA and DNA-binding proteins (V, VII, μ) in the viral core [9].

Like many other viruses, adenovirus undergoes a final maturation step driven by a virus encoded protease (reviewed in [10]). Pulse-chase experiments established that several of the viral structural peptides are synthesized in a precursor form, while the mature, infective particle contains the cleaved products. The agent responsible for proteolytic maturation is the viral L3 23 K protein or adenovirus protease (AVP) [11]. AVP recognizes (M/I/L)XGX-G and (M/I/L)XGG-X sequence motifs to cleave minor capsid proteins IIIa, VI and VIII, as well as DNA binding proteins VII, μ, and the terminal protein (TP) [12]. Such cleavages result in a total mass of more than 6 MDa cleaved peptides in the 150 MDa virion (**Table 1**), that might be expected to change location or organization during virion maturation. The putative scaffolding protein L1 52/55K has a sequence cleavage motif at residue 351 (LAGT-G) and also appears to be cleaved during maturation; however, whether the AVP is responsible for L1 52/55K processing is not clear, as this protein is absent from the mature particles and present in very few copies in immature, DNA containing virions [13]. The C-terminal peptide of precursor polypeptide pVI (pVI_C), released upon cleavage by AVP, and the

viral dsDNA, act as cofactors and increase the protease catalytic rate by several orders of magnitude [14; 15; 16; 17]. It has also been reported that precursor pVI, but not mature VI, acts as a carrier to transport newly synthesized hexon to the nucleus [18], via interaction of a nuclear localization signal located in the pVI_C peptide with importin α/β.

A classic human adenovirus type 2 (Ad2) thermosensitive mutant (Ad2 *ts1*) is deficient in proteolytic processing [19]. When grown at the non-permissive temperature (39°C), Ad2 *ts1* does not package the viral protease [20], and produces capsids containing the unprocessed protein precursors. Viral genome packaging is unimpaired, but the virus is not infectious. It has been shown that the defect in infectivity is linked to a defect in uncoating. Immature Ad2 *ts1* attaches to the host cell and follows the same internalization process as the wild type virus, but is not able to escape the endosome and is recycled to the membrane or degraded in lysosomes [21; 22]. On the other hand, wild type virus treated with protease inhibitors can proceed all the way to the nuclear pore, but fails to release its DNA [22]. Coimmunoprecipitation of fiber with hexon after different periods of endocytosis indicated that fiber release is much less efficient in immature Ad2 *ts1* than in wild type virus, even after treatment with protease inhibitors [22], while kinetics studies indicated that immature Ad2 *ts1* accumulated a disassembly intermediate containing core components [23]. Proper release of polyeptide VI from the uncoating virion seems to be required to disrupt the endosomal membrane [24].

Other large icosahedral dsDNA viruses, most notably herpesvirus and tailed bacteriophage, undergo maturation by proteolytic processing [25]. This process is

generally coupled with DNA packaging, and involves large rearrangements of the capsid building blocks. On the other hand, no such maturation process has been described for the structural counterpart of adenovirus in the bacteriophage world, the membrane-containing PRD1, or any other of the PRD1-adenovirus lineage members [26]. The only changes reported for PRD1 correspond to an increase in capsid-membrane contacts upon DNA packaging [27; 28].

Here we report comparison of the structure and uncoating behavior of immature Ad2 *ts1* and wild type viruses, studies undertaken to address the following questions: what are the structural rearrangements involved in proteolytic maturation? What is the location of the uncleaved peptides in the capsid? And, how do the structural differences relate to differences in infectivity?

Results

Structure of mature and immature capsids

Using cryo-electron microscopy (cryo-EM) data, we have obtained 3D density maps for wild type and immature (Ad2 *ts1* grown at 39ºC) adenovirus at approximately 9 Å resolution (**Fig. 1**). To detect possible fine changes in the relative position of capsomers between the mature and immature particles, the crystal structures of hexon and penton base were independently fitted to the wild type and *ts1* maps, to obtain a quasi-atomic model for each viral species (**Fig. 1**). The RMSD between the molecules fitted to the wild type and *ts1* maps was 2.64 Å for the 11048 C-α atoms in the icosahedral asymmetric unit (AU). This RMSD was mainly due to a ~2 Å shift along the virus radius of the whole AU, consistent with the fitting accuracy on a 9 Å resolution map. There were no evident large scale rearrangements, or significant changes in the relative rotation between capsomers.

Difference mapping: localization of unprocessed peptides

Detailed inspection of the 3DEM maps revealed two main differences between the mature and immature virus capsids. First, a well defined feature appeared beneath some hexons in the *ts1* map, at the interface between capsid and core (type 1 difference; **Fig. 2,** boxes). Second, diffuse extra density filled the inner cavities of all hexon trimers in *ts1* (type 2 difference; **Fig. 2,** circles; also visible in **Fig. 1A**). These differences were better interpreted by making use of difference maps. The difference

map between the wild type cryo-EM map and its quasi-atomic model, containing only the hexon and penton base structures, revealed the molecular envelopes corresponding to minor coat proteins IX, IIIa, and VIII, as well as fiber and hexon loops not present in the crystal structure (**Fig. 2B and D,** yellow). Overlaying this map with that calculated by subtracting the wild type from the *ts1* virus cryo-EM maps (**Fig. 2 B and D,** red) showed the location of the main differences between the mature and immature capsids with respect to the densities assigned to minor capsid components in the current model for the wild type virus [7].

Sixty copies (one per AU) of type 1 difference density (**Fig. 2**, boxes) were found underneath the vertex region, intercalated between the five arms of a star formed by the densities corresponding to polypeptide IIIa and one of the two independent copies of polypeptide VIII in the AU. At this position, the type 1 difference is within contact range of multiple capsid components: polypeptides IIIa and VIII, hexons 1 (peripentonal) and 2 (close to the 2-fold axis) in one AU, and hexon 4 in the adjacent AU across the icosahedral edge (**Fig. 2B**). The type 1 difference is therefore making a bridge between two icosahedral facets, and between the ring of peripentonal hexons and those making the central plate of the facet, known as the group-of-nine (GON). Because of its position, the type 1 difference could arise from the uncleaved C-terminal fragments of polypeptide VIII or IIIa. The mass of the type 1 difference peak, when measured at 1.25 σ contour level, is 2.1 kDa. This is much closer to the expected value for the C-terminal polypeptide IIIa peptide ($IIIa_C$, 1.8 kDa) than to the expected value for the polypeptide VIII C-terminal fragment (12.6 kDa, **Table 1**). At the same contour level, the calculated mass for the N-terminal fragment of VIII (**Fig. 2B, star**) is 10.8 kDa, in reasonable agreement with the expected value (12.1 kDa).

Furthermore, no similar difference density was found close to the second independent copy of polypeptide VIII in the AU (**Fig. 2B, star**). This evidence indicates that the type 1 difference is more likely to correspond to a part of the pIIIa precursor that to the C-terminal fragment of pVIII.

Extra density (type 2 difference, circles in **Fig. 2**) was found inside all hexon cavities in the *ts1*-wild type difference map. This is the position proposed for polypeptide VI in the current adenovirus capsid model [7]. The average mass of the 4 independent type 2 peaks in the AU is 0.9 ± 0.2 kDa. Therefore, type 2 difference can be attributed to either the uncleaved pVI C-terminal peptide (1.3 kDa, **Table 1**), or to a larger structural order in the precursor *vs.* the processed polypeptide. For hexons 2, 3 and 4, this extra density appears at medium height in the cavity, close to a hexon loop previously shown to be involved in interaction with VI [18]. In the peripentonal hexons (green in **Fig. 2B and D**), however, type 2 difference reaches to the innermost region in the cavity (**Fig. 2D**). This region of the hexon trimer is highly acidic (**Fig. 2E**), suggesting a role for electrostatic interactions between capsid components. Similar charge-rich regions (although basic in this case) have been found in the internal cavity of the trimeric major coat protein of bacteriophage PRD1 and *Paramecium bursaria Chlorella* virus type 1 (PBCV-1), both members of the adenovirus structural lineage, and proposed to interact with minor capsid components [29; 30]. Interestingly, both polypeptide VI and its precursor pVI present basic isoelectric point values (9.6 and 9.9 respectively), while the AVP cofactor pVI_C has an even more basic character when considered separately (pI=11.7).

Apart from those underneath the vertex region and inside the central hexon cavities, no other significant differences were observed between the wild type and *ts1* icosahedral protein shells. There was no difference at the external side of the capsid, nor was there any negative difference density in the *ts1*-wild type map that could account for the presence of protease in the mature virus.

Core organization

Adenovirus cryo-EM maps do not provide information on the organization of DNA and DNA-binding proteins in the viral core, because this part of the particle does not follow icosahedral symmetry. Nevertheless, a difference was observed between the wild type and *ts1* 3D maps at the core level. While in the wild type map the weak core density follows the icosahedral profile of the capsid, the *ts1* core presents a somewhat more spherical profile (**Fig. 1**). Radial average plots showed that core density is stronger for *ts1* than for wt, particularly in the first layer beneath the icosahedral shell (**Fig. 3A**). This indicates a more compact or more ordered state for the immature core. Further evidence for a difference in core organization and stability was found from the occasional observation of disrupted virions in *ts1* cryo-EM preparations. In these particles the icosahedral protein shell peels away, leaving behind a well defined spherical particle of approximately 650 Å diameter. This disruption pattern is not observed for the wild type virus, where the contents of broken capsids show a much more diffuse aspect (**Fig. 3B**).

Disassembly assays

Some broken viral particles like those described above appear routinely in virus preparations, but the reason for their disruption is not known. Therefore, we tried to characterize the different disassembly patterns for mature and immature virions under more controlled conditions. Structural changes in viruses subject to increasingly higher temperatures (15 to 80ºC) were monitored by two different techniques. DNA exposure to the solvent was measured by the increase in fluorescence of propidium iodide (PI) when bound to DNA, while disassembly products were imaged by negative staining electron microscopy.

When DNA release was measured as a function of temperature, the fluorescence pattern of mature and immature viruses indicated a different behavior (**Fig. 4A**). The first sharp increase in fluorescence occurred at 45ºC for wild type virus, but was delayed until 47ºC for *ts1*. Fluorescence became more intense at a consistently slower rate for *ts1* than for wild type, until a plateau was reached at 60ºC for wild type and 65ºC for *ts1*. Our results differ from previous fluorescence studies on DNA release, in which very little change in TOTO-1 fluorescence was observed for *ts1* under a range of pH and temperature [24]. Our experimental conditions vary from those reported by Wiethoff and collaborators in the lower ionic strength (15 *vs.* 100 mM NaCl) and the presence of EDTA. Low ionic strength has been shown to reduce adenovirus stability [31], while chelation of divalent cations by EDTA loosens core compaction [32]. Both conditions may have facilitated detection of *in vitro* disassembly intermediates not previously observed, as shown below.

When the disassembly products were examined by electron microscopy, the most conspicuous difference between wild type and *ts1* appeared for samples heated in the

45-50ºC range (**Fig. 4B**). In wild type sample, we observed broken capsids forming planar, open hexon arrays of different sizes, while cores appeared as untidy filamentous bundles with a relatively compact center. Conversely, in *ts1* preparations at 45 and 47ºC the protein shell retained its spherical arrangement, with openings consistent with loss of pentons and the peripentonal hexon ring, or of larger parts of the capsid. These holey shells contained a spherical, compact core, from which a single filament projected. This filament is thicker (12.3 ± 2.3 nm, N=50) that those protruding from wild type cores (5.3 ± 1.5 nm, N=100), indicating a different protein coating for the released DNA.

Discussion

Viral capsid components fulfill many different roles during the infectious cycle, among them recognition of assembly partners in the crowded host cell, virion stabilization against conditions in the extracellular milieu, and release of viral genome upon entry. Changes in their organization during the maturation process are often used for switching among functions and ensure the generation of a final, infectious particle. In tailed bacteriophage, and the structurally related herpesvirus, this process has been extensively studied and shown to involve large rigid body movements of capsomers, together with capsid expansion required to accommodate the packaged genome [25]. Other DNA viruses, like papillomavirus, seem to follow the opposite direction, with a compaction of the procapsid required to achieve stability [33]. Finally, the bacteriophage representative of the adenovirus lineage, PRD1, maintains capsid size and organization during the transition from the empty protein-membrane shell to the final virion [27; 28]. It is therefore not surprising that the capsid structure of immature adenovirus, as revealed here by a 9 Å resolution 3DEM map of the Ad2 *ts1* mutant, presents only relatively small differences with that of the wild type, mature virus.

What, then, are the changes produced by proteolytic processing of many adenovirus polypeptides that result in an incorrect uncoating behavior, and therefore a lack of infectivity? We observed differences in the structure of immature *vs.* mature adenovirus at two levels: as additional ordered elements in the icosahedral protein shell, and as a general reorganization of the core. These differences may act together to produce the differential uncoating behavior that we have observed by biophysical methods and by direct imaging using the electron microscope.

AVP cleaves minor capsid proteins IIIa, VI, and VIII. We find difference peaks in our *ts1*-wild type maps at two positions in the capsid: the periphery of a highly helical structure forming a cartwheel underneath the vertex region, and inside the hexon trimer cavity oriented towards the virus core. According to the current adenovirus capsid model [7], the rim of the cartwheel underneath the vertex is formed by a tight overlap of polypeptides IIIa and VIII. Our type 1 difference density, located at this rim, could arise from either of the two proteins. However, the peak size, and the fact that a similar difference peak does not appear close to the second independent copy of polypeptide VIII in the AU, indicates that type 1 difference is most likely originated by the $pIIIa_C$ peptide. This structural element must play a role in increasing the network of interactions required for capsid assembly, and in hindering adequate uncoating of immature virus. Its position suggests that it is acting as a molecular stitch, riveting together two adjacent facets in the icosahedrons, as well as fastening the peripentonal ring to the GONs. As in the case of a surgical stitch, this structure would be removed by the protease action when no longer needed, allowing uncoating to proceed. Evidence for the importance of polypeptide IIIa in adenovirus capsid architecture has already been reported. Ad2 *ts112* mutant, with three point mutations in IIIa, accumulates empty particles [34; 35]; and only small, unstructured peptides were tolerated as N-terminal extensions in IIIa [8]. Our findings reveal one more aspect of the key, multifunctional role of this minor coat protein during assembly.

The current adenovirus capsid model locates polypeptide VI in the internal cavity of the hexon trimer, which would attribute our type 2 difference peak to its precursor pVI. The assignment of polypeptide VI to a location inside the hexon trimer is

problematic, since the copy number of VI, estimated around 360, is too low to have one molecule of VI per hexon monomer (copy number 720), and too high to have one VI per hexon trimer (copy number 240). The weak difference density between the wild type cryo-EM map and the quasi atomic model at this position has been interpreted as arising from partial occupancy [7] in a 1:1 hexon-VI interaction. The appearance of a difference peak inside the cavity of all four hexon trimers in the AU of our *ts1*-wild type map, at reasonably high density levels, indicates an increased icosahedral ordering in the pVI precursor. The strong negative charge of the hexon cavity, together with the basic character of pVI_C, and the type 2 difference peak size, make it very tempting to interpret this difference density as the 11-residue peptide. However, such a sequestered location would appear to hinder interaction of AVP (packaged with the DNA) with its second cofactor [15; 17], as well as the proposed interaction with the nuclear import machinery to aid in hexon nuclear import [18]. On the other hand, one could hypothesize that this putative electrostatic interaction would be important for the carrier function of pVI, while its perturbation by cleavage of pVI_C would be the trigger to facilitate polypeptide VI release and therefore endosomal escape.

Apart from polypeptides IIIa, VI and VIII, AVP also cleaves core proteins VII, μ, and TP. Since the viral core does not follow icosahedral symmetry, it is not possible to analyze differences in this region using icosahedral cryo-EM reconstructions. However, both analysis of the *ts1* 3D map and direct observation of virions by electron microscopy indicate a different, more structured and stable core organization for the immature particle. These properties may result, at least in part, from differences in the interactions of protein VII and its precursor with the viral genome:

an N-terminal sequence of pVII, but not of mature protein VII can efficiently crosslink to viral DNA in intact particles [36]. Another core component, polypeptide μ, is extensively proteolyzed from its 80 residue precursor to a final 19 residue peptide. Studies showing that mature polypeptide μ can precipitate dsDNA from solution suggested that this small peptide could have a role in condensing the viral genome to fit it into the capsid shell [37]. It is possible that this function is enhanced by the uncleaved pre-μ amino and carboxy-terminal extensions, either via direct interactions with the viral genome or with other core components, to keep the viral genome in a stable form during morphogenesis. Further connection between pre-μ and virus stability has been found in an Ad5 variant lacking polypeptide V, where a thermosensitive phenotype was rescued by a cluster of mutations in the N-terminal fragment of the immature polypeptide [38].

The differences in capsid and core structure we observe correlate with a different *in vitro* disassembly behavior for mature and immature capsids and cores when the virion is subject to heat treatment. An “all or nothing” disruption pattern was found for wild type virus, with completely disordered capsids and cores at 45 ºC. The immature virus, on the contrary, seemed to follow a slower, sequential disassembly process, going through loss of pentons and peripentonal hexons and partial, well ordered unraveling of protein-coated DNA. This unraveling pattern is consistent with the asymmetric DNA packing determined by the location of packaging specific sequences at the left end of the viral genome [39], and may also correlate with the presence of a singular, specialized vertex structure in the otherwise icosahedral shell [40]. There is currently uncertainty regarding the mode of adenovirus DNA packaging, since evidence exists to support both concerted and sequential assembly and

packaging [41; 42]. One intriguing question arises from our observations on the immature core: how can such a compact organization be reconciled with DNA packaging through a single vertex into the empty procapsid?

In conclusion, our findings indicate that three main players participate in modulating the stability switch required to go from adenovirus assembly to uncoating. First, a molecular stitch formed by $pIIIa_C$ increases capsid stability during assembly by riveting together adjacent facets and the ring of peripentonal hexons. Second, electrostatic interactions between pVI_C and hexon may hamper release of polypeptide VI and therefore endosomal escape. And third, a tighter organization of DNA and DNA binding proteins pVII and pre-μ in the core would hinder passage through the nuclear pore and bar access of the cellular transcriptional machinery to the viral genome.

Note: while this manuscript was under review, a 10.5 Å resolution cryoEM study of Ad2 *ts1* was reported [43]. These authors also note a stronger core signal in the immature virus, compatible with increased icosahedral order or with higher density. They also observe that in their *ts1* 3D map the density gap usually found between the icosahedral shell and the non-icosahedral core disappears. This is interpreted by Silvestry and co-workers as the immature core being more ordered, but less condensed, than the mature one. This is at variance with our results, where the same gap is present in the wild type and *ts1* 3D maps, and images of disrupted virions clearly show a much more condensed state in the immature core.

Materials and Methods

Virus production and purification. We used as control wild type, mature virions the E1-deleted human adenovirus type 5 (Ad5) variants Ad5GL, Ad5Luc1-HFpIIIa, and Ad5GLflagIIIa, previously described in [44] and [8]. Ad5GL is completely wild type for all structural polypeptides, while Ad5Luc1-HFpIIIa and Ad5GLflagIIIa encode small peptides (approximately 20 residues) fused to the N-terminus of polypeptide IIIa. Viruses were propagated in HEK293 cells, purified as previously described [8], and stored at -70ºC in PBS (8 mM Na_2HPO_4, 2 mM KH_2PO_4, 137 mM NaCl, and 2.7 mM KCl [pH 7.4]) plus 10% glycerol. Virus titers were $5x10^{12}$ (Ad5GL), $1x10^{12}$ (Ad5Luc-HFpIIIa), and $4x10^{12}$ (Ad5GLflagIIIa) part/ml. Immature virus was obtained by propagating the Ad2 *ts1* mutant in HeLa cells at 39.5º. Particles were purified by equilibrium centrifugation in CsCl gradients, desalted on a 10DC column (Bio-Rad) and stored in 20 mM Hepes pH 7.8, 150 mM NaCl plus 10% glycerol at -70ºC at a final concentration of $1x10^{13}$ part/ml.

Cryo-electron microscopy. Virus samples were dialyzed for 1 hour at 4ºC against PBS, applied to freshly carbon-coated, glow discharged Quantifoil R2/4 300 mesh Cu/Rh grids, and vitrified in liquid ethane using a Leica CPC plunger. Grids were mounted in a Gatan 626 cryostage and examined in a FEI Tecnai G2 FEG microscope operating at 200 kV. Micrographs were recorded on Kodak SO-163 film under low dose conditions at a nominal magnification of 50,000x, and digitized in a Zeiss Photoscan TD scanner using a step size of 7 µm (1.4 Å in the sample).

Three-dimensional reconstruction. All image processing and three-dimensional reconstruction tasks were performed using the software package XMIPP [45; 46], except for determination of micrograph contrast transfer function (CTF) parameters which was done with CTFFIND [47]. Micrographs free of drift and astigmatism (290 for wild type, 297 for *ts1*) were selected and downsampled to a final pixel size of 2.8 Å/px. Particles were manually picked, extracted into 408x408 pixel boxes, normalized, and corrected for the phase oscillations of the CTF (phase flip). Images were automatically sorted into defocus groups covering a range between -0.5 and -5.8 µm for wild type, -0.5 and -5.1 µm for *ts1*. Iterative projection matching against a previously obtained 14 Å resolution wild type Ad5 map [8] was carried out using an algorithm designed to efficiently calculate the test orientations for very fine angular steps (Marabini, Scheres *et al*., in preparation). Orientation searches were performed with decreasing angular steps, from 2 degrees to a final 0.2 degrees; correction of the CTF amplitudes was performed using Wiener filtering; and 3D reconstruction was performed using interpolation in Fourier space [48]. Icosahedral symmetry was imposed throughout the refinement process. The final datasets included 9018 (wild type) and 9621 (*ts1*) particles. Fourier shell correlation (FSC) with a threshold of 0.3 gave a resolution of 8.9 Å (wild type) and 8.7 Å (*ts1*). At FSC = 0.5, the corresponding resolution values were 9.7 and 9.5 Å. A temperature factor of approximately -450 $Å^2$ was calculated according to [49] and applied to the final maps to enhance high resolution features. Enhanced maps were low-pass filtered to the calculated resolution, and grayscale normalized within radii 294 to 490 Å, roughly enclosing the icosahedral capsid shell. The mature and immature virus 3DEM maps have been deposited at the Macromolecular Structure Database (MSD,

http://www.ebi.ac.uk/msd) with accession codes EMD-1579 and EMD-1586, respectively.

Fitting of high resolution structures and calculation of difference maps. Starting from the previously reported adenovirus quasi-atomic model (PDB ID 2BLD, [6]), the crystal structures of four hexon trimers and one penton base molecule were fitted into our wild type and immature virus maps using URO [50], with icosahedral symmetry enforced. Since the Ad5 and Ad2 hexon structures are practically identical [2], the Ad5 hexon (PDB ID 1P30) was used for both maps. The scale of the maps was refined during fitting, giving a final pixel size of 2.76 Å. This scale was used to calculate the various difference maps. RMSD values between the fitted AU for wild type and *ts1* were calculated with LSQMAN [51]. A 9 Å resolution density map was calculated from the fitted hexon and penton base crystal structures, using EMAN PBD2MRC [52]. Difference maps revealing those capsid components other than hexon and penton base were calculated by subtracting this map from the cryo-EM reconstructions. Another difference map was calculated by subtracting the wild type cryo-EM map from that of the *ts1* mutant. Surface rendering figures were created with UCSF Chimera [53], using the Hide Dust tool to remove small, unconnected blobs from the difference maps. All maps were contoured at the same level (1.25σ after grayscale normalization within the icosahedral shell). Difference peak mass values were calculated by measuring their volumes at 1.25σ level with Chimera, and considering an average protein density of 1.33 g/cm^3. The electrostatic potential of a hexon trimer was calculated with the PyMol (http://www.pymol.org/) APBS plug-in [54] and visualized with Chimera.

Disassembly assays. Mature and immature virus samples ($5x10^{10}$ part/ml) were incubated at different temperatures in 8 mM Na_2HPO_4, 2 mM KH_2PO_4, 15mM NaCl, 0.1mM EDTA, pH=7.4 with 1 mM propidium iodide (Molecular Probes). Fluorescence emission spectra were obtained employing a Hitachi Model F-2500 FL Spectrophotometer equipped with a cell holder and Peltier temperature control device. A 10-min equilibration time was used at each temperature before data acquisition. Sample volumes of 0.150 ml were examined in sealed quartz cuvettes. The sample was excited at 535 nm and the emission was monitored from 580 to 700 nm using excitation and emission slit widths of 8 nm. The fluorescence intensity near the wavelength of maximum fluorescence intensity for each spectrum (607 nm) was plotted as a function of temperature. The spectra were corrected by subtraction of the buffer spectrum at each corresponding temperature. PI maximum intensities for each temperature are presented as a fraction of the initial maximum (I/Io) with standard errors (N=3). For imaging of disassembly products, samples were adsorbed to glow discharged, collodion/carbon coated EM grids, negatively stained with 2% uranyl acetate, and observed in a Jeol 1200EX-II transmission electron microscope.

Acknowledgements

This work was supported by grants from the Ministerio de Ciencia e Innovación of Spain (BFU2007-60228 to C. S. M. and BIO2007-67150-C03-03 to R. M.); the Comunidad Autónoma de Madrid and Consejo Superior de Investigaciones Científicas (CCG08-CSIC/SAL-3442 to C. S. M.); and National Institutes of Health (5R01CA111569 to D. T. C.; R0141599 to W. F. M.; and GM037705 to S. J. F.). R. M.-C. is a recipient of a PFIS fellowship from the Instituto de Salud Carlos III of Spain.

We are grateful to María López (CNB-CSIC) and Wenying Huang (Princeton University) for technical assisstance; and Dr. Daniel Luque (CNB-CSIC) for help with URO. We acknowledge use of computing resources at the Supercomputing Center of Galicia (CESGA).

References

1. Zubieta, C., Schoehn, G., Chroboczek, J. & Cusack, S. (2005). The structure of the human adenovirus 2 penton. *Mol Cell* **17**, 121-35.
2. Rux, J. J., Kuser, P. R. & Burnett, R. M. (2003). Structural and phylogenetic analysis of adenovirus hexons by use of high-resolution x-ray crystallographic, molecular modeling, and sequence-based methods. *J Virol* **77**, 9553-66.
3. van Raaij, M. J., Mitraki, A., Lavigne, G. & Cusack, S. (1999). A triple β-spiral in the adenovirus fibre shaft reveals a new structural motif for a fibrous protein. *Nature* **401**, 935-8.
4. Xia, D., Henry, L. J., Gerard, R. D. & Deisenhofer, J. (1994). Crystal structure of the receptor-binding domain of adenovirus type 5 fiber protein at 1.7 Å resolution. *Structure* **2**, 1259-70.
5. Stewart, P. L., Fuller, S. D. & Burnett, R. M. (1993). Difference Imaging of Adenovirus - Bridging the Resolution Gap between X-Ray Crystallography and Electron-Microscopy. *EMBO Journal* **12**, 2589-2599.
6. Fabry, C. M., Rosa-Calatrava, M., Conway, J. F., Zubieta, C., Cusack, S., Ruigrok, R. W. & Schoehn, G. (2005). A quasi-atomic model of human adenovirus type 5 capsid. *EMBO J* **24**, 1645-54.
7. Saban, S. D., Silvestry, M., Nemerow, G. R. & Stewart, P. L. (2006). Visualization of α-helices in a 6 Å resolution cryoEM structure of adenovirus allows refinement of capsid protein assignments. *J Virol* **80**, 12049-12059.
8. San Martín, C., Glasgow, J. N., Borovjagin, A. V., Beatty, M. S., Kashentseva, E. A., Curiel, D. T., Marabini, R. & Dmitriev, I. P. (2008). Localization of the N-terminus of minor coat protein IIIa in the adenovirus capsid. *J Mol Biol* **383**, 923-34.

9. San Martín, C. & Burnett, R. M. (2003). Structural studies on adenoviruses. In *Adenoviruses: Model and Vectors in Virus Host Interactions. Current Topics in Microbiology and Immunology* (Doerfler, W. & Böhm, P., eds.), Vol. 272, pp. 57-94. Springer-Verlag, Heidelberg.

10. D´Halluin, J. C. (1995). Virus assembly. *Curr Top Microbiol Immunol* **199**, 47-66.

11. Weber, J. M. (1999). Role of endoprotease in adenovirus infection. In *Adenoviruses : basic biology to gene therapy* (Seth, P., ed.), pp. 79-83. R.G. Landes, Austin, Tex., U.S.A.

12. Diouri, M., Keyvani-Amineh, H., Geoghegan, K. F. & Weber, J. M. (1996). Cleavage efficiency by adenovirus protease is site-dependent. *J Biol Chem* **271**, 32511-4.

13. Hasson, T. B., Ornelles, D. A. & Shenk, T. (1992). Adenovirus L1 52- and 55-kilodalton proteins are present within assembling virions and colocalize with nuclear structures distinct from replication centers. *J Virol* **66**, 6133-42.

14. Baniecki, M. L., McGrath, W. J., McWhirter, S. M., Li, C., Toledo, D. L., Pellicena, P., Barnard, D. L., Thorn, K. S. & Mangel, W. F. (2001). Interaction of the human adenovirus proteinase with its 11-amino acid cofactor pVIc. *Biochemistry* **40**, 12349-56.

15. Mangel, W. F., McGrath, W. J., Toledo, D. L. & Anderson, C. W. (1993). Viral DNA and a viral peptide can act as cofactors of adenovirus virion proteinase activity. *Nature* **361**, 274-5.

16. Mangel, W. F., Toledo, D. L., Brown, M. T., Martin, J. H. & McGrath, W. J. (1996). Characterization of three components of human adenovirus proteinase activity *in vitro*. *J Biol Chem* **271**, 536-43.

17. McGrath, W. J., Baniecki, M. L., Li, C., McWhirter, S. M., Brown, M. T., Toledo, D. L. & Mangel, W. F. (2001). Human adenovirus proteinase: DNA binding and stimulation of proteinase activity by DNA. *Biochemistry* **40**, 13237-45.

18. Wodrich, H., Guan, T., Cingolani, G., Von Seggern, D., Nemerow, G. & Gerace, L. (2003). Switch from capsid protein import to adenovirus assembly by cleavage of nuclear transport signals. *EMBO J* **22**, 6245-55.

19. Weber, J. (1976). Genetic analysis of adenovirus type 2 III. Temperature sensitivity of processing viral proteins. *J Virol* **17**, 462-71.

20. Rancourt, C., Keyvani-Amineh, H., Sircar, S., Labrecque, P. & Weber, J. M. (1995). Proline 137 is critical for adenovirus protease encapsidation and activation but not enzyme activity. *Virology* **209**, 167-73.

21. Cotten, M. & Weber, J. M. (1995). The adenovirus protease is required for virus entry into host cells. *Virology* **213**, 494-502.

22. Greber, U. F., Webster, P., Weber, J. & Helenius, A. (1996). The role of the adenovirus protease in virus entry into cells. *EMBO J* **15**, 1766-77.

23. Mirza, M. A. & Weber, J. (1979). Uncoating of adenovirus type 2. *J Virol* **30**, 462-71.

24. Wiethoff, C. M., Wodrich, H., Gerace, L. & Nemerow, G. R. (2005). Adenovirus protein VI mediates membrane disruption following capsid disassembly. *J Virol* **79**, 1992-2000.

25. Steven, A. C., Heymann, J. B., Cheng, N., Trus, B. L. & Conway, J. F. (2005). Virus maturation: dynamics and mechanism of a stabilizing structural transition that leads to infectivity. *Curr Opin Struct Biol* **15**, 227-36.

26. Krupovic, M. & Bamford, D. H. (2008). Virus evolution: how far does the double beta-barrel viral lineage extend? *Nat Rev Microbiol* **6**, 941-8.

27. Butcher, S. J., Bamford, D. H. & Fuller, S. D. (1995). DNA packaging orders the membrane of bacteriophage PRD1. *EMBO J.* **14**, 6078-86.

28. San Martín, C., Burnett, R. M., de Haas, F., Heinkel, R., Rutten, T., Fuller, S. D., Butcher, S. J. & Bamford, D. H. (2001). Combined EM/X-ray imaging yields a quasi-atomic model of the adenovirus-related bacteriophage PRD1, and shows key capsid and membrane interactions. *Structure* **9**, 917-930.

29. San Martín, C., Huiskonen, J. T., Bamford, J. K., Butcher, S. J., Fuller, S. D., Bamford, D. H. & Burnett, R. M. (2002). Minor proteins, mobile arms and membrane-capsid interactions in the bacteriophage PRD1 capsid. *Nat Struct Biol* **9**, 756-63.

30. Nandhagopal, N., Simpson, A. A., Gurnon, J. R., Yan, X., Baker, T. S., Graves, M. V., Van Etten, J. L. & Rossmann, M. G. (2002). The structure and evolution of the major capsid protein of a large, lipid-containing DNA virus. *Proc Natl Acad Sci U S A* **99**, 14758-63.

31. Rexroad, J., Evans, R. K. & Middaugh, C. R. (2006). Effect of pH and ionic strength on the physical stability of adenovirus type 5. *J Pharm Sci* **95**, 237-47.

32. Harpst, J. A., Ennever, J. F. & Russell, W. C. (1977). Physical properties of nucleoprotein cores from adenovirus type 5. *Nucleic Acids Res* **4**, 477-90.

33. Buck, C. B., Thompson, C. D., Pang, Y. Y., Lowy, D. R. & Schiller, J. T. (2005). Maturation of papillomavirus capsids. *J Virol* **79**, 2839-46.

34. D'Halluin, J. C., Milleville, M., Boulanger, P. A. & Martin, G. R. (1978). Temperature-sensitive mutant of adenovirus type 2 blocked in virion assembly: accumulation of light intermediate particles. *J Virol* **26**, 344-56.

35. Chroboczek, J., Viard, F. & D'Halluin, J. C. (1986). Human adenovirus 2 temperature-sensitive mutant 112 contains three mutations in the protein IIIa gene. *Gene* **49**, 157-60.

36. Chatterjee, P. K., Yang, U. C. & Flint, S. J. (1986). Comparison of the interactions of the adenovirus type 2 major core protein and its precursor with DNA. *Nucleic Acids Res* **14**, 2721-35.

37. Anderson, C. W., Young, M. E. & Flint, S. J. (1989). Characterization of the adenovirus 2 virion protein, mu. *Virology* **172**, 506-12.

38. Ugai, H., Borovjagin, A. V., Le, L. P., Wang, M. & Curiel, D. T. (2007). Thermostability/infectivity defect caused by deletion of the core protein V gene in human adenovirus type 5 is rescued by thermo-selectable mutations in the core protein X precursor. *J Mol Biol* **366**, 1142-60.

39. Hearing, P., Samulski, R. J., Wishart, W. L. & Shenk, T. (1987). Identification of a repeated sequence element required for efficient encapsidation of the adenovirus type 5 chromosome. *J Virol* **61**, 2555-8.

40. Christensen, J. B., Byrd, S. A., Walker, A. K., Strahler, J. R., Andrews, P. C. & Imperiale, M. J. (2008). Presence of the adenovirus IVa2 protein at a single vertex of the mature virion. *J Virol* **82**, 9086-93.

41. Ostapchuk, P. & Hearing, P. (2005). Control of adenovirus packaging. *J Cell Biochem* **96**, 25-35.

42. Finnen, R. L., Biddle, J. F. & Flint, J. (2001). Truncation of the human adenovirus type 5 L4 33-kDa protein: evidence for an essential role of the carboxy-terminus in the viral infectious cycle. *Virology* **289**, 388-99.

43. Silvestry, M., Lindert, S., Smith, J. G., Maier, O., Wiethoff, C. M., Nemerow, G. R. & Stewart, P. L. (2009). Cryoelectron microscopy structure of the adenovirus type 2 temperature sensitive mutant 1 reveals insight into the cell entry defect. *J. Virol.*, JVI.00331-09.

44. Seki, T., Dmitriev, I., Kashentseva, E., Takayama, K., Rots, M., Suzuki, K. & Curiel, D. T. (2002). Artificial extension of the adenovirus fiber shaft inhibits infectivity in coxsackievirus and adenovirus receptor-positive cell lines. *J Virol* **76**, 1100-8.

45. Sorzano, C., Marabini, R., Velázquez-Muriel, J., Bilbao-Castro, J., Scheres, S., Carazo, J. & Pascual-Montano, A. (2004). XMIPP: a new generation of an open-source image processing package for electron microscopy. *J Struct Biol.* **148**, 194-204.

46. Scheres, S. H., Núñez-Ramírez, R., Sorzano, C. O., Carazo, J. M. & Marabini, R. (2008). Image processing for electron microscopy single-particle analysis using XMIPP. *Nat Protoc* **3**, 977-90.

47. Mindell, J. A. & Grigorieff, N. (2003). Accurate determination of local defocus and specimen tilt in electron microscopy. *J Struct Biol* **142**, 334-47.

48. Li, Y., Kummert, A., Boschen, F. & Herzog, H. (2008). Interpolation-based reconstruction methods for tomographic imaging in 3D positron emission tomography. *International Journal of Applied Mathematics and Computer Science* **18**, 63-73.

49. Rosenthal, P. B. & Henderson, R. (2003). Optimal determination of particle orientation, absolute hand, and contrast loss in single-particle electron cryomicroscopy. *J Mol Biol* **333**, 721-45.

50. Navaza, J., Lepault, J., Rey, F. A., Alvarez-Rua, C. & Borge, J. (2002). On the fitting of model electron densities into EM reconstructions: a reciprocal-space formulation. *Acta Crystallogr D Biol Crystallogr* **58**, 1820-5.

51. Kleywegt, G. J., Zou, J. Y., Kjeldgaard, M. & Jones, T. A. (2001). Around O. In *International Tables for Crystallography* (Rossmann, M. G. & Arnold, E., eds.), Vol. F. Crystallography of Biological Macromolecules. Chapter 17.1, pp. 353-356. Kluwer Academic Publishers, The Netherlands, Dordrecht.

52. Ludtke, S. J., Baldwin, P. R. & Chiu, W. (1999). EMAN: semiautomated software for high-resolution single-particle reconstructions. *J Struct Biol* **128**, 82-97.

53. Pettersen, E. F., Goddard, T. D., Huang, C. C., Couch, G. S., Greenblatt, D. M., Meng, E. C. & Ferrin, T. E. (2004). UCSF Chimera--a visualization system for exploratory research and analysis. *J Comput Chem* **25**, 1605-12.

54. Baker, N. A., Sept, D., Joseph, S., Holst, M. J. & McCammon, J. A. (2001). Electrostatics of nanosystems: application to microtubules and the ribosome. *Proc Natl Acad Sci U S A* **98**, 10037-41.

Figure Legends

Fig 1. 3DEM maps and quasi-atomic models. Central sections of the wild type **(A)** and *ts1* **(B)** maps, both filtered at 8.9 Å resolution. The bar represents 200 Å. Higher density is white. **(C)** Resolution assessment. Fourier shell correlation curves for the wild type (**wt**) and *ts1* 3DEM maps. **(D)** Surface rendering showing the wild type AU, as seen from outside the virion. The 4 independent hexon trimers are labeled 1-4. Hexon 1 and its symmetry mates form the peripentonal ring; hexon trimers 2, 3 and 4 form the GONs. The bar represents 100 Å. **(E)** Ribbon representation showing the wild type quasi-atomic AU model. The four hexon trimers have been labeled as in (D) and depicted in different colors to facilitate interpretation. One penton base molecule is shown in dark blue. **(F)** A slab of the AU showing the good correspondence between the cryoEM density (semitransparent surface) and α-helices at the base of the hexon trimers, colored as in (E). Black filled symbols indicate the 5-fold (pentagon), 3-fold (triangle) and 2-fold (oval) icosahedral symmetry axes.

Fig 2. Differences between mature and immature capsids. **(A)** Details of sections (42 Å away from the virion center, looking along a 2-fold axis as in Fig. 1 A and B) of the wild type (wt) and *ts1* 3DEM maps, as indicated. The positions of extra densities appearing in the *ts1* map are indicated with a white square (type 1 difference, at the capsid-core interface) and circle (type 2 difference, inside the hexon cavity). **(B)** Surface rendering of the wild type-quasi atomic model (yellow) and *ts1*-wild type (red) difference maps superimposed on the quasi-atomic model density map (semitransparent). Note that the AU is shown as seen from inside the virus, i.e. rotated 180º around a horizontal axis with respect to Fig. 1D, E and F. The four independent hexon trimers and one penton base molecules are colored as in Fig. 1E. Black boxes and circles indicate the location of type 1 and type 2 difference densities. Black filled stars indicate the position of the second independent polypeptide VIII copy (the first one is located underneath the peripentonal ring). Black filled symbols indicate the 5-fold (pentagon), 3-fold (triangle) and 2-fold (oval) icosahedral symmetry axes. **(C)** Schematics showing an AU in the same orientation as in (B). The four hexon trimers are represented as hexagons, and the penton base as a pentagon. Black and grey shapes indicate the current model assignments for polypeptides IIIa, VI and VIII. Red boxes and circles indicate the location of the *ts1*-wild type type 1 and 2 differences. **(D)** A section across the icosahedral edge showing the inner cavities of hexon trimers 1 (green) and 2 (purple). External density in the wild type-quasi-atomic difference map (yellow) corresponds to the fiber (**f**) and hexon loops (**hl**). Colors and symbols as in (B). **(E)** Electrostatic surface coloring for a hexon trimer. The front half of the molecule has been clipped away to reveal charges within the cavity. All scale bars represent 50 Å.

Fig 3. Differences between mature and immature cores. **(A)** Radial average profile of the wild type and *ts1* 3DEM maps. **(B)** Examples of disrupted virions found in cryo-EM preparations of wild type (**wt**) and *ts1* samples, as indicated. An arrow indicates an intact particle. The scale bar represents 100 nm.

Fig 4: Disassembly assays. **(A)** Analysis of DNA release for wild type and *ts1* virus measured by extrinsic PI fluorescence at 607 nm as a function of temperature. Average values and error bars indicating standard deviations for triplicate measurements are plotted. **(B)** Negative stain electron microscopy images of wild type and *ts1* disassembly intermediates obtained at 45 or 47ºC, as indicated. The scale bar represents 200 nm.

Table 1. Adenovirus polypeptides cleaved by AVP. Residue numbers refer to Ad2 sequence. Shadowed rows indicate peptides with a strong tendency to structural disorder, as predicted by FOLDINDEX [54].

Polypeptide	Precursor length (aa)	Cleaved peptides	Peptide mass (kDa)	Approximate copy number	Total peptide mass in virion (kDa)	Disorder prediction (FOLDINDEX)
IIIa	585	570-585	1.8	60	108	yes
VI	250	1-33	3.6	360	1296	no
		239-250	1.3	360	468	yes
VII	198	1-24	2.6	800	2080	yes
VIII	227	112-227[3]	12.6	120	1512	no
μ	80	1-32	3.4	100	340	yes
		51-80	2.9	100	290	no
TP	653	Not clear[1]	32[2]	2	64	?

[1] Four potential sites predicted by PattinProt [55].

[2] Estimated from the difference in mass between the precursor (87 kDa) and the final product (55 kDa).

[3] The C-terminal fragment of polypeptide VIII is considered, as the N-terminal fragment has previously been assigned to ordered density in the wildtype capsid [7]. PattinProt predicts two more cleavage sites, at residue numbers 131 and 157.

Figure1

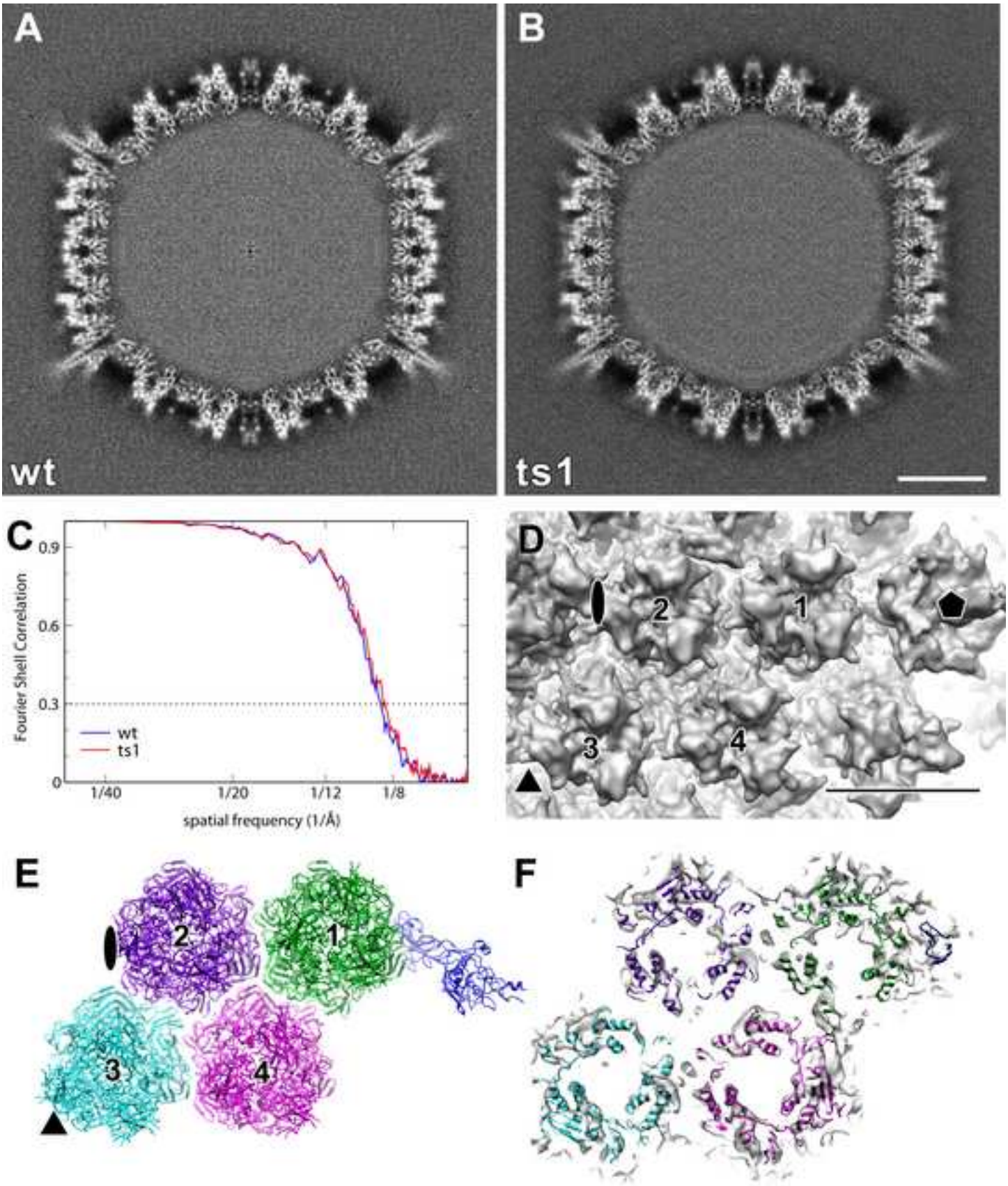
A
wt
B
ts1
C
Fourier Shell Correlation
0.9
0.6
0.3
0
wt
ts1
1/40
1/20
1/12
1/8
spatial frequency (1/Å)
D
1
2
3
4
E
1
2
3
4
F

Figure2

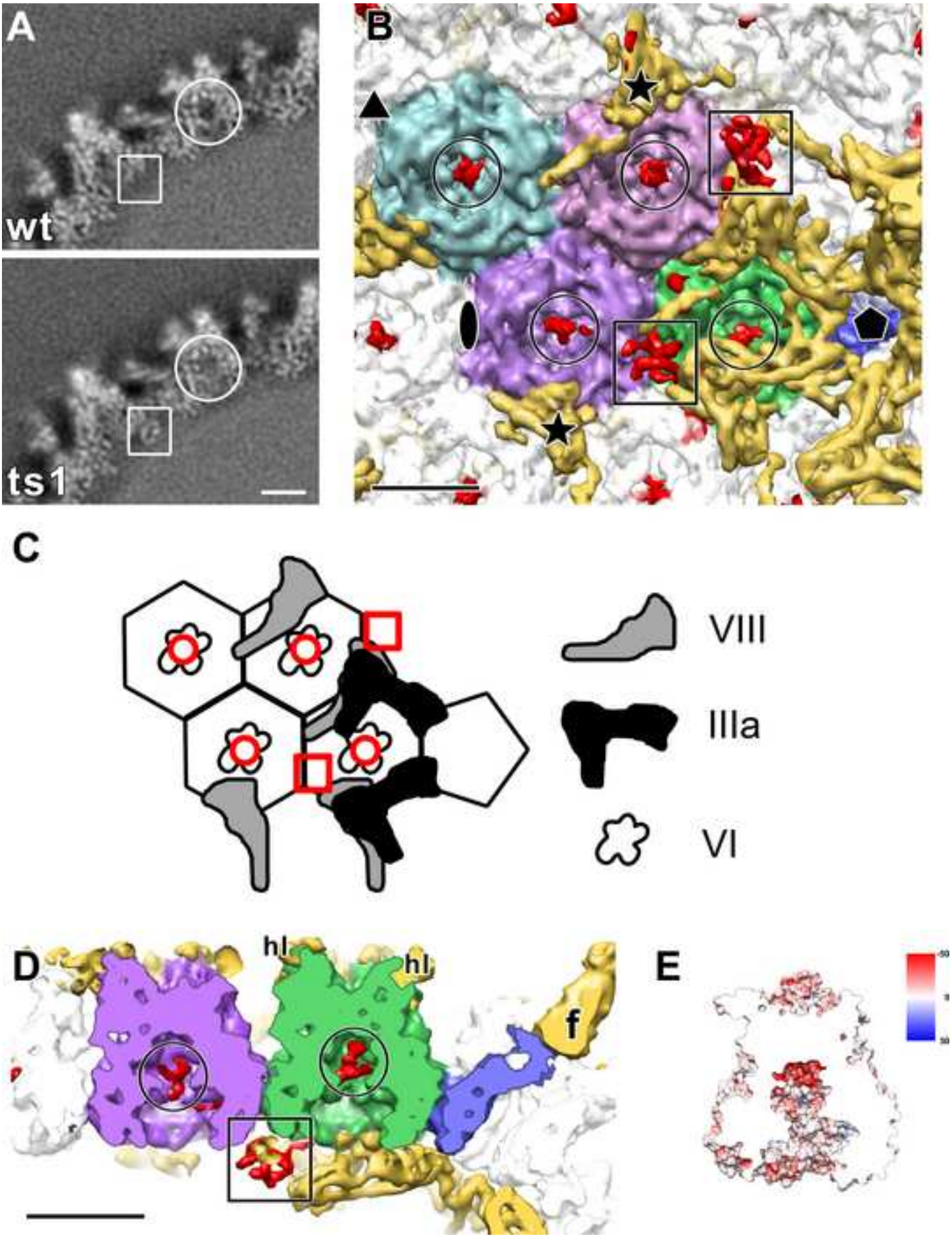

Figure3

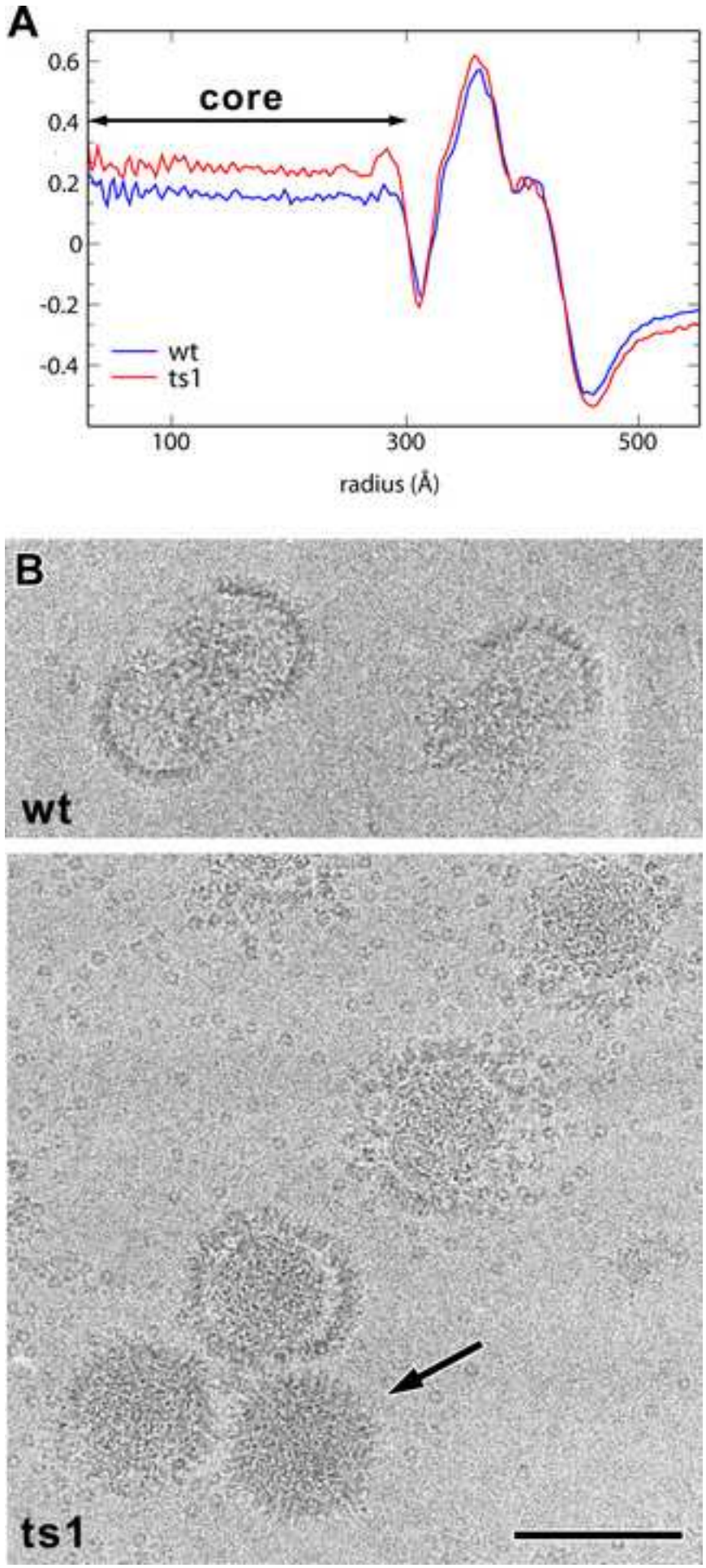

Figure4